Full length article

3D multicellular model of shock wave-cell interaction

Dongli Li *, Andre Hallack, Robin O. Cleveland *, Antoine Jérusalem *

University of Oxford, Department of Engineering Science, Parks Rd., Oxford OX1 3PJ, UK

ABSTRACT

Understanding the interaction between shock waves and tissue is critical for advancing the use of shock waves for medical applications, such as cancer therapy. This work aims to study shock wave-cell interaction in a more realistic environment, relevant to *in vitro* and *in vivo* studies, by using 3D computational models of healthy and cancerous cells. The results indicate that for a single cell embedded in an extracellular environment, the cellular geometry does not influence significantly the membrane strain but does influence the von Mises stress. On the contrary, the presence of neighbouring cells has a strong effect on the cell response, by increasing fourfold both quantities. The membrane strain response of a cell converges with more than three neighbouring cell layers, indicating that a cluster of four layers of cells is sufficient to model the membrane strain in a large domain of tissue. However, a full 3D tissue model is needed if the stress evaluation is of main interest. A tumour mimicking multicellular spheroid model is also proposed to study mutual interaction between healthy and cancer cells and shows that cancer cells can be specifically targeted in an early stage tumour-mimicking environment.

Statement of Significance

This work presents 3D computational models of shock-wave/cell interaction in a biophysically realistic environment using real cell morphology in tissue-mimicking phantoms and multicellular spheroids. Results show that cell morphology does not strongly influence the membrane strain but influences the von Mises stress. While the presence of neighbouring cells significantly increases the cell response, four cell layers are enough to capture the membrane strain change in tissue. However, a full tissue model is necessary if accurate stress analysis is needed. The work also shows that cancer cells can be specifically targeted in early stage tumour mimicking environment. This work is a step towards realistic modelling of shock-wave/cell interactions in tissues and provides insight on the use of 3D models for different scenarios.

1. Introduction

Shock waves have been clinically used to fragment kidney stones for many decades in a procedure called lithotripsy [1]. Shock waves are also used to treat musculoskeletal disorders including calcific tendonitis of the shoulder as well as non-unions and delayed unions of long bone fractures [2]. Other clinical applications for shock waves include histotripsy which incites a localised cavitation cloud to mechanically fractionate tissue [3] and shock wave mediated drug delivery and gene transfer for cancer treatment [4]. A critical issue for these shock wave applications is that side-effects on the healthy tissue are often found during and after the treatment. Therefore minimising damage on healthy tissues around the therapeutic target has been the focus of many research studies.

Recently, we presented a combined experimental/numerical method which captures the shock wave interaction with a single cell embedded in a tissue mimicking phantom [5]. Two shortcomings of the model were that the cells were modelled as spheres and were embedded in a homogeneous tissue-mimicking gel without neighbouring cells, which may not realistically represent cells *in vitro* and *in vivo*.

In this work, we aim to analyse how cell morphology and the presence of neighbouring cells influence the cell response to shock waves. This is a step towards a realistic computational model for shock wave interactions with cells in tissue.

Section 2 presents the experimental analysis of cell morphology inside a tissue-mimicking phantom and a cluster. The analysis

serves as the basis for the models presented in Sections 3 and 4 to study the influence of cell morphology and neighbouring cells on shock wave-cell interaction.

2. Experimental study

Individual real cell models were constructed in 3D based on fluorescent images of the cell membrane using multiphoton microscopy (MPM). A fluorescent imaging experiment was also performed on a cell monolayer for comparing its cell morphology to that in a multicellular spheroid.

2.1. Cell sample preparation

An immortalised human kidney epithelial cell line, HK-2 (ATCC CRL-2190), was used in this study. The cells were cultured according to the protocols in a sterile environment [6]. The tissue-mimicking phantom was made of a mixture of 0.6% purified agarose solution (UltraPure Agarose, Invitrogen), 0.1 million HK-2 cells and cell media (DMEM, Sigma-Aldrich Ltd.). This composition provides an elastic modulus of ~10 kPa and density of ~1000 kg/m^3 which are similar to the mechanical properties observed in soft tissues [7]. The low cell density and homogeneous distribution in the tissue phantom allow for the imaging of individual cells. The phantom was held in a 12-well plate with a thickness of less than 5 mm for imaging purposes.

2.2. Multiphoton microscopy (MPM)

MPM was used to obtain the detailed real cell geometries for rendering the 3D cell morphologies used in the simulations. MPM uses two or more low-energy photons excitation to cause higher energy electronic transition in a fluorescent molecule, which allows for high resolution and high contrast fluorescent images in thick samples [8]. A bespoke MPM was used which employs a focussed laser tunable from 700 nm to 1000 nm to scan over the tissue samples. In the experiment, stacks of 512 × 512 pixels images were taken for three different HK-2 cells embedded in the tissue phantom with an image slice interval of 300 nm. A nuclear acid stain (Hoechst 33342, Life Technologies) and a plasma membrane stain (Cellmask, Life Technologies) were used to label the cell nucleus and cortex membrane, respectively. Each tissue

sample in the 12-well plate was submerged with the diluted Cellmask solution with 1.5× concentration in the incubator for 30 min to allow the staining solution to diffuse through the gel matrix. The staining solution was then replaced with the Hoechst staining solution with concentration of 0.2 μg/mL after washing the sample three times with a physiologically relevant buffer. The samples were then incubated for another 30 min for the cell nucleus to be labelled. An example of the fluorescent image slice is shown in Fig. 1(a) where the blue colour labels the cell nucleus and red labels the cell membrane.
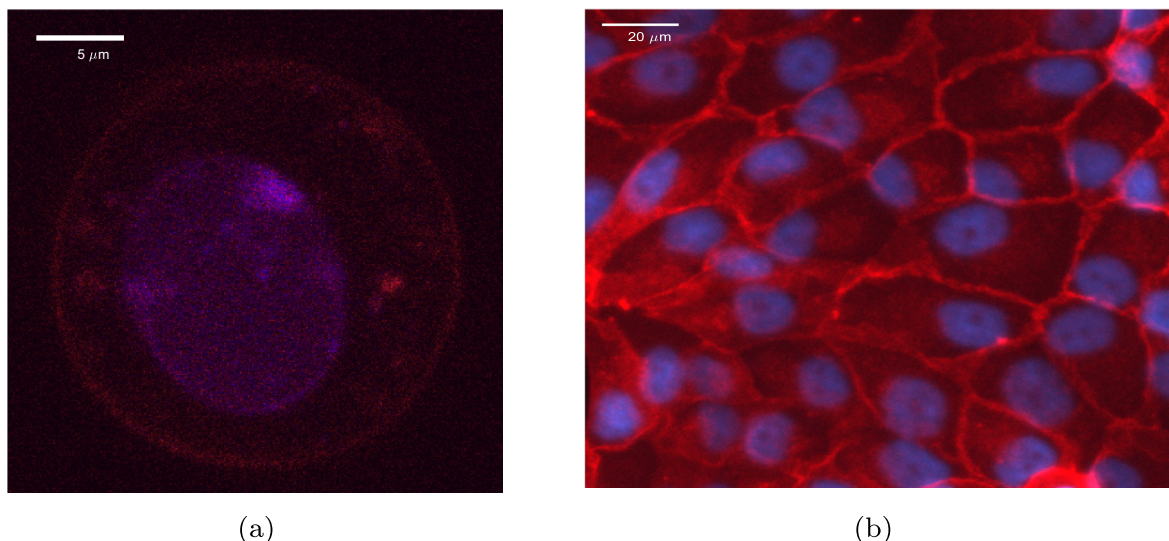
2.3. Cell cluster imaging

0.5 mL HK-2 cell suspension containing 10,000 cells was placed on a cover slip inside a 24-well plate for 1 h. After the cells reached 80% confluency on the cover slip, the cells were fixated with 4% paraformaldehyde solution for 15 min and stained through the same protocol as for the single cell imaging. Fluorescent imaging was performed using an inverted optical microscope (Nikon, Eclipse Ti) with a 20× microscopic objective, see Fig. 1(b).

3. Cellular numerical framework

3.1. Model setup

Previous work [9] modelled individual neurons with a differentiation of some representative subcellular compartments (i.e., nucleus, cytoplasm and cortical membrane). However, our experimental setup for the cells of interest makes it impossible to identify the mechanical properties of these different cell components. The literature for such properties under shock loading is also missing. As a first approximation, the cells are thus modelled as a homogeneous solid with a shell cortical membrane. The cortical membrane was modelled with a thickness of 200 nm, and meshed with shell elements. The thickness of the cortical membrane was chosen as the lower bound value in the variation of cortical membrane thickness found in Ref. [10]. The single cell models were embedded in a homogeneous tissue-mimicking environment. Shock waves were applied at the top surface of the tissue model. The shock wave profiles (Fig. 2) were determined from measurements by a bespoke fibre-optic probe hydrophone (FOPH) [11] inside an agarose tissue phantom at three different shock wave

(a) (b)

Fig. 1. (a) A slice of MPM image of single cell embedded in the agarose gel; (b) fluorescent image of HK-2 cell monolayer on cover slip. Cell membrane and nucleus are labelled in red and blue, respectively. (For interpretation of the references to colour in this figure legend, the reader is referred to the web version of this article.)

energy levels. The simulations were performed in the explicit dynamic solver of the software Abaqus (Dassault Systèmes) with linear tetrahedral elements. The mechanical cell response was analysed in terms of von Mises stress for shearing evaluation and cell damage indication, and the overall membrane strain which indicates the change of membrane permeability for drug delivery applications. The membrane strain was calculated as the cell surface area change over time. More details on the model are presented in the SI.

3.1.1. Constitutive material framework

The material laws employed in the model simulate the volumetric and deviatoric behaviours separately.

$$\boldsymbol{\tau} = \boldsymbol{\tau}_{vol} + \boldsymbol{\tau}_{dev} \tag{1}$$

The deviatoric response of the cell model ($\boldsymbol{\tau_{dev}}$) was described by a nonlinear viscoelastic constitutive framework while the volumetric response ($\boldsymbol{\tau}_{vol} = Jp\mathbf{I}$) was simulated by an Equation of State (EoS) using a bilinear bulk modulus calibrated against experimental observations [5].

Nonlinear viscoelasticity: The employed first order nonlinear viscoelasticity framework [12] can be further decomposed into the initial elastic response τ° and the evolution of viscous stress $\boldsymbol{\tau_{vis}}$:

Fig. 2. Shock wave pressure profiles measured inside agarose tissue phantom using a FOPH; different colors represent the pressure profile at different shock wave energy levels: levels 4, 6 and 8.

$$\tau_{dev} = \tau^\circ + \tau_{vis}$$

$$= \gamma_\infty \text{dev}\{2\partial_{\bar{\mathbf{C}}}W^\circ[\bar{\mathbf{C}}(t)]\} + \gamma_1 \text{dev}\{\bar{\mathbf{F}}(t)\int_{-\infty}^{t} \exp[-(t-s)/\tau_1]$$

$$\times \frac{d}{ds}\bar{\mathbf{F}}(s)^{-1}\text{dev}\{2\partial_{\bar{\mathbf{C}}}\bar{W}^\circ[\bar{\mathbf{C}}(s)]\bar{\mathbf{F}}(s)^{-T}\}ds\,\bar{\mathbf{F}}(t)^T\} \tag{2}$$

where "dev" is the deviator operator: $dev[\cdot] = (\cdot) - \frac{1}{3}[(\cdot):\mathbf{I}]\mathbf{I}$, $\bar{\mathbf{F}}$ and $\bar{\mathbf{C}}$ are the volume-preserving deformation gradient and right Cauchy-Green tensors, τ_1 is the relaxation time of the viscoelastic component, which is the ratio between viscosity and shear modulus (i.e., $\tau_1 = \eta_1/\mu_1$) and γ_1 is the proportion of the shear modulus of the viscous component to the instantaneous shear modulus (i.e., $\gamma_1 = \mu_1/(\mu_\infty + \mu_1)$).

Equation of state: During compression the bulk modulus is taken to be K_C but during tension when the pressure exceeds a transition density threshold, $\tilde{\rho}$, the bulk modulus reduces to K_T:

$$p = \text{H}(\tilde{\rho} - \rho)\left(K_T \frac{\rho - \rho_0}{\rho_0} + \Delta p\right) + \text{H}(\rho - \tilde{\rho})K_C \frac{\rho - \rho_0}{\rho_0} \tag{3}$$

where H is the Heaviside function, K_C and K_T are the bulk moduli corresponding to compression and tension, respectively, $\Delta p = (K_C - K_T)(\tilde{\rho} - \rho_0)/\rho_0$, $\tilde{\rho}$ is the transition density, and ρ_0 is the density at initial state. See Ref. [5] for more details.

Table 1 lists the mechanical properties of different human kidney epithelial cells calibrated in the previous study [5] where a high speed imaging experiment was performed to visualise the deformation of each single cell subject to shock waves in order to measure its mechanical properties. The surrounding tissue-mimicking phantom was modelled as a nonlinear elastic material with EoS accounting for its volumetric response.
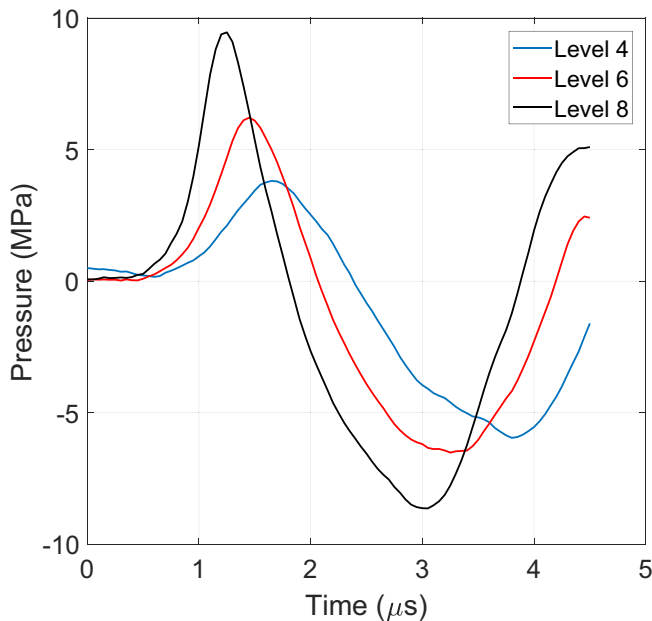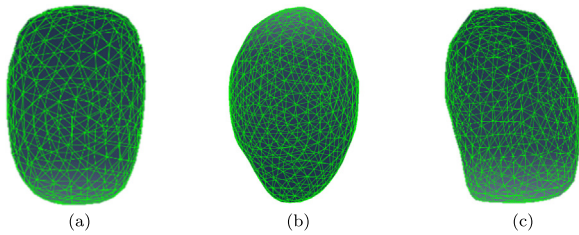
3.1.2. Cell shape variability

The influence of the cell shape was studied by constructing cell models from the MPM images of three arbitrarily selected individual cells: for each MPM fluorescent slice, the cell membrane was semi-automatically segmented based on the intensity threshold using Amira [17], a commercial 3D software for visualisation and meshing. The 3D volume of the cell was thus rendered and meshed in Amira. The three cell models constructed from real cell geometries are presented in Fig. 3.

The cell response from different cell models were compared with each other and with a spherical model with radius of 10 μm, a mean value of HK-2 cell radius found in the cell size distribution experiment, see SI for more details.

3.1.3. Cell orientation variability

In order to study the influence of the cell orientation, one of the reconstructed cell models (cell sample 2, Fig. 3(b)) was rotated by 45°, 90°, 135° and 180° polar angles (Fig. 4).

Table 1
Material properties of the three different cell lines (HK-2, CAKI-2 and HRE), cell membrane and tissue-mimicking phantom.

Cell	Cell type	K_C	K_T	$\tilde{\rho}$	μ_∞	μ_1	η_1
[5,13,14]	HK-2	2 GPa	20 MPa	−4.6 MPa	3.1 kPa	0.34 kPa	69.6 Pa·s
	CAKI-2	2 GPa	34 MPa	−4 MPa			
	HRE	2 GPa	25 MPa	−4.6 MPa			
Membrane		K			μ_∞	μ_1	η_1
[14,15]		2 GPa			333.34 Pa	13.89 Pa	41.67 kPa·s
Tissue phantom		K			μ		
[16]		2 GPa			3.45 kPa		

Fig. 3. Cell models constructed from real HK-2 cell geometries: (a) sample 1; (b) sample 2 and (c) sample 3.

3.2. Single cell simulation results

3.2.1. Influence of cell shape

The effect of cell shape variability on cell response was found to be similar between different shock wave energy levels. Therefore, only the cell response at shock wave energy level 6 (medium level) is presented to illustrate the influence of cell shape on cell response. More simulation results at other shock wave energy levels can be found in the SI.

Fig. 5(a) compares the von Mises stress at the distal part of each cell model (away from the shock wave source) where the cell shape changes most dramatically. The highest von Mises stress was found in the HK-2 cell sample 2 which has the sharpest curvature (Fig. 3 (b), mean curvature 0.2884); while the cell model exhibiting the flattest bottom (HK-2 cell sample 1, mean curvature 0.0944) showed the smallest von Mises stress. The mean curvature of the models are calculated from the surface curvature algorithms [18]. A higher mean curvature value indicates a more acute surface curvature. More details are explained in the SI.

Fig. 5(b) shows that different real cell models exhibited similar overall membrane strain: the membrane strains in the three real cell models were around 3.5% with a variation of less than 5%; the spherical model showed a larger membrane strain (~4.5%) which deviated from the mean membrane strain of the real cell models by 15%. In addition, the influence of cell sizes on the shock wave-cell interaction was also found to be small (<20% variation), see SI.
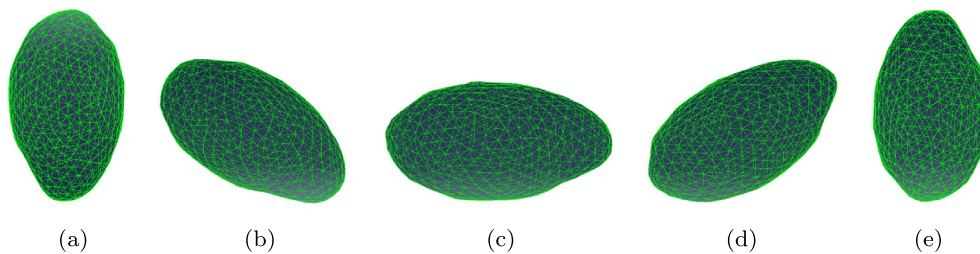
3.2.2. Influence of cell orientation

The von Mises stresses at the cell bottom and the cell membrane strain measured at shock wave energy level 6 for all five orientations of cell sample 2 are shown in Fig. 6. The cell response was consistent with the finding in the cell shape analysis: the von Mises stresses were related to the model curvature at the measurement point, therefore the cell model rotated by 90° showed the smallest von Mises stress while the largest value was found in the nonrotated state. The respective mean surface curvature of each oriented cell model is illustrated in the SI. The membrane strain showed variations of less than 2%, indicating no significant difference under the effect of model orientations.
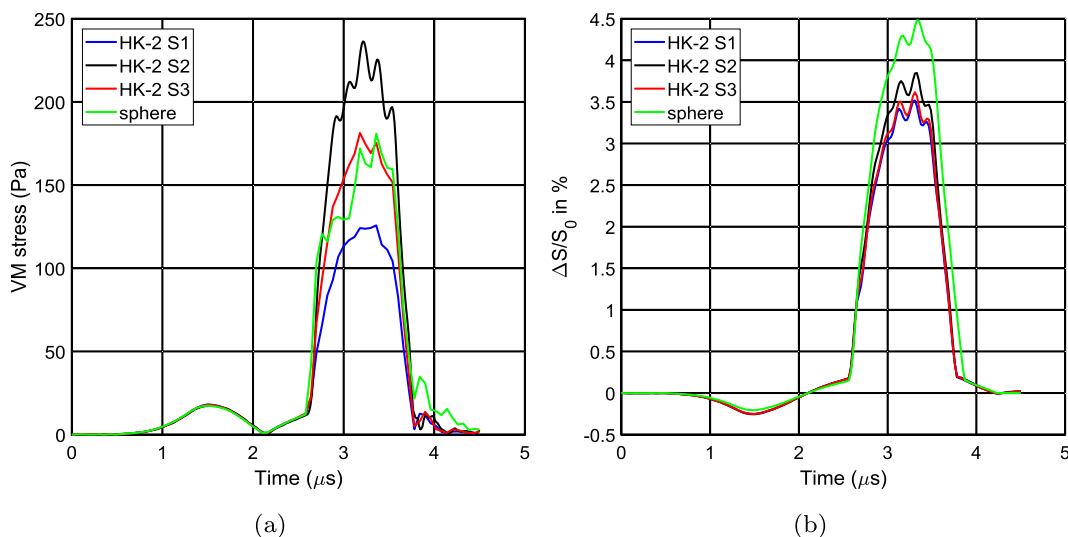
4. Multicellular spheroid numerical study

4.1. Model description

In order to investigate the influence of neighbouring cells, a multicellular spheroid model was constructed using generalised Voronoï tessellations. Voronoï tessellations have been applied to model cell-cell and cell-matrix adhesion as well as 3D tissue
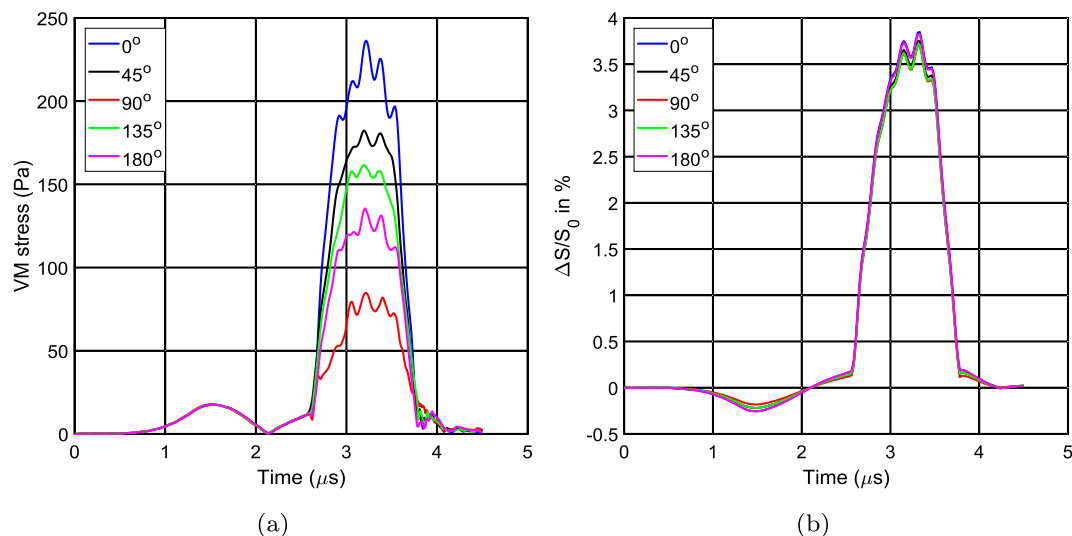

Fig. 4. Cell model constructed from sample 2 with varying orientations: (a) 0°, (b) 45°, (c) 90°, (d) 135° and (e) 180° polar angles.

Fig. 5. Cell response due to the influence of cell shapes. (a) von Mises stress measured at the distal part of the cell; (b) membrane strain.

Fig. 6. Cell response in each orientation model: 0°, 45°, 90°, 135° and 180°. (a) von Mises stress measured at the distal part of the cell; (b) membrane strain.

[19,20]. The open source program Neper [21] was used to generate a Voronoï tessellation assembling for the cell cluster in a spherical domain of a diameter of 200 μm containing 300 cells. Each cell was separated and connected through its cortical membrane modelled as a viscoelastic material [14], see Table 1. As a first approximation, the interface between two cells was modelled as one common cortical membrane of 200 nm thickness. An analysis of the influence of this thickness on the main results did not show significant variability (mean variability <20% for von Mises stress and 5% for membrane strain).

4.1.1. Cell spheroid models

The individual cells in the spheroid model were modelled with the material properties from HK-2 cells, see Table 1. The spheroid model was split into a number of submodels constructed layer-by-layer around the central single cell in order to study the effect of each layer of neighbouring cells on the centre cell response, see Fig. 7. The cross-sectional view of the spheroid models are similar to the image of HK-2 cell monolayer (Fig. 1(b)) in which the cells are also comparable to that inside an early stage 3D multicellular spheroid, see confocal images of tightly connected cells in Ref. [22].
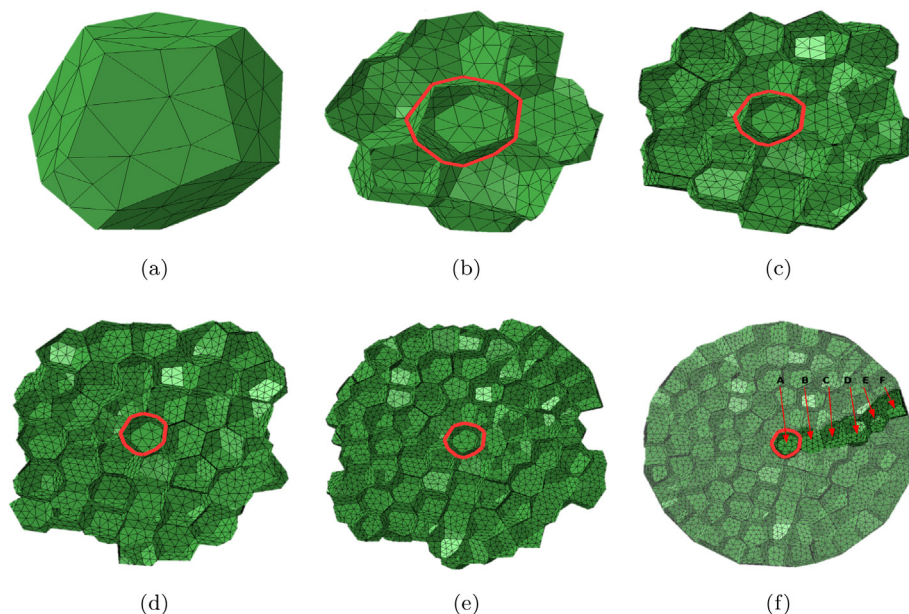
In the full spheroid model (Fig. 7(f)), a representative cell in each ring layer was selected to study the cell response distribution at different parts of the cluster.

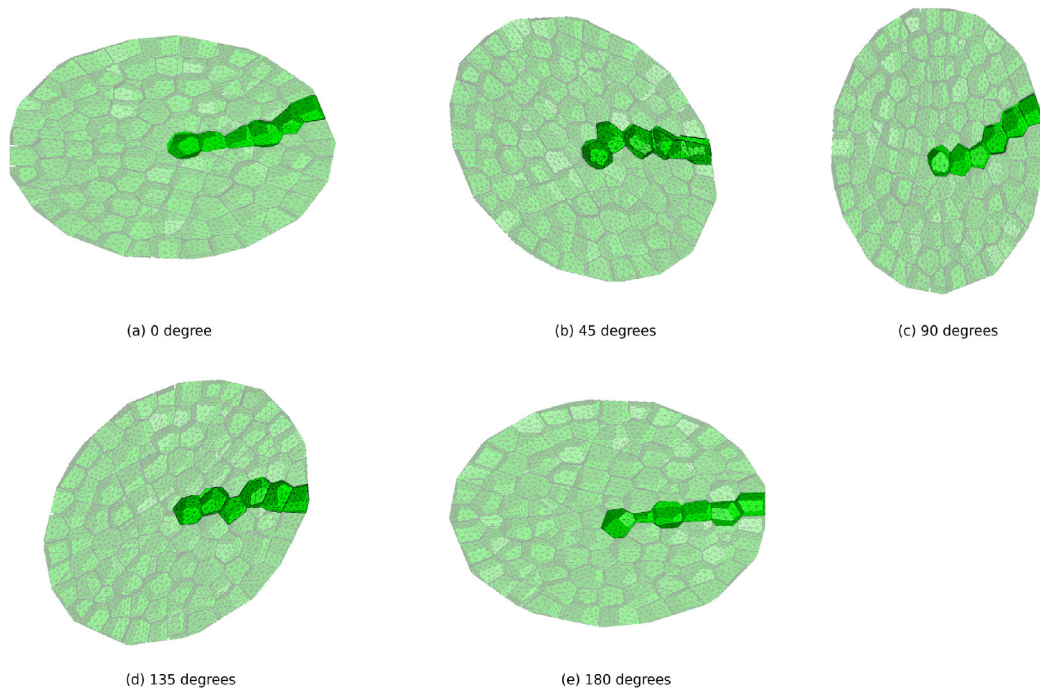### 4.1.2. Change of cluster morphology and orientations

In order to study the influence of cluster morphology and orientation, the full spheroid model was uniaxially stretched by 30% and rotated by 45°, 90°, 135° and 180°. A representative cell in each ring layer was selected. Fig. 8 presents the morphologically changed spheroid models for all rotational angles.
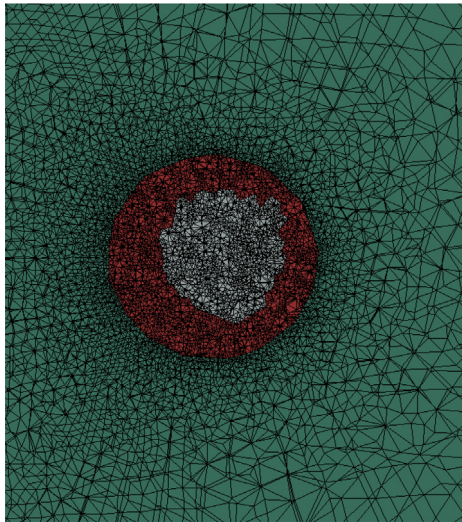
4.1.3. Tumour mimicking model

A model mimicking an initial tumour growth was built by using the mechanical properties of normal healthy (HRE) cells on the outer 2 layers while modelling the inner 3–4 layers of the spheroid

Fig. 7. Spheroid models by layers. (a) no surrounding layers; (b) with one surrounding layer; (c) with two surrounding layers; (d) with three surrounding layers; (e) with four surrounding layers; (f) full spheroid model (with 5–6 surrounding layers). The red line labels the central cell and A to F labels the representative cell for each layer.

(a) 0 degree

(b) 45 degrees

(c) 90 degrees

(d) 135 degrees

(e) 180 degrees

Fig. 8. Spheroid model stretched by 30% and rotated by 0° (a), 45° (b), 90° (c), 135° (d) and 180° (e) with respect to the shock wave propagation direction. The representative cells for the cluster centre and each ring later are highlighted.

Fig. 9. A spheroid model with differentiated inner cluster of cancer cells (white) and the surrounding normal cells (red). (For interpretation of the references to colour in this figure legend, the reader is referred to the web version of this article.)

with cancer (CAKI-2) cells (see Fig. 9). The mechanical properties of the HRE and CAKI-2 cells are given in Table 1.

4.2. Simulation results

4.2.1. Influence of neighbouring cells

The spheroid was subject to an incident shock wave at shock wave energy level 6. Fig. 10 shows the response of the central cell as a function of the number of layers of cells around it. The presence of neighbouring cell layers resulted in an increase of von Mises stress and membrane strain in comparison to that of an isolated cell embedded in the tissue phantom. The von Mises stress in

the compressive phase did not change significantly with the number of cell layers. In comparison, the von Mises stress in the tensile phase exhibited a delay in the occurrence of the peak stress of up to 2 μs and a four-fivefold increase in amplitude. This is due to the fact that the lower cell bulk modulus for tension results in slower wave propagation speed. The membrane strain was more than doubled when neighbouring cells were present. The membrane strain evolution curves converge for more than three surrounding layers, revealing around 8% membrane strain increase compared to 2.5% in the no-surrounding layers case.

4.2.2. Response of representative cells of each ring layer

Fig. 11 shows the response of the representative cell of each ring layers in the full spheroid model (Fig. 7(f)). The membrane strain showed relatively homogeneous distribution in the spheroid as the computed waveforms were similar in different representative cells. However, the von Mises stress was higher in the spheroid centre (∼600 Pa) compared to the surrounding layers (∼200 Pa). This may be caused by the geometrical accumulation of stress waves propagating in the spheroid.

4.2.3. Influence of cluster morphology and orientations

Fig. 12. shows the comparison of the representative cell response of each ring layer between the original model and its morphologically stretched counterpart. The morphology change of the spheroid model was found to influence the distribution of the von Mises stress resulting in 37.8% of mean variability. This may be caused by the change of stress wave interference patterns due to the change of cluster morphology. The influence on cell membrane strain is relatively smaller, resulting in 17.8% of mean variability, mainly on the outer layers of the cluster which are less constrained compared to the cluster centre. See SI for more details.

Fig. 13. shows the von Mises stress and membrane strain of each representative cell for the different rotation cases. While the orientation of the spheroid does not heavily influence the membrane strain of individual cells, the von Mises stress is strongly
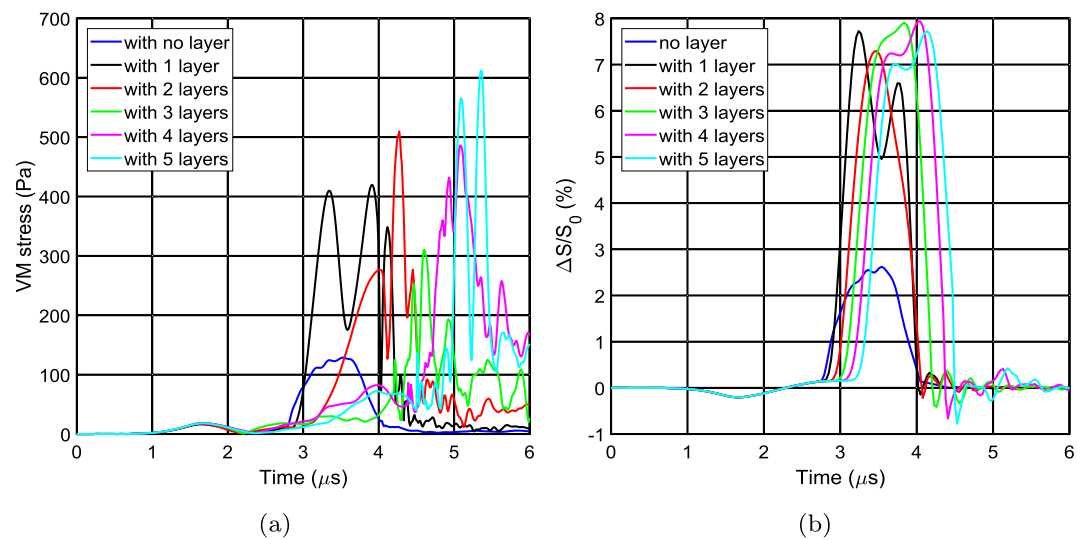
Fig. 10. Central cell response for different cluster sizes: (a) von Mises stress measured at the distal part of the cell; (b) membrane strain.
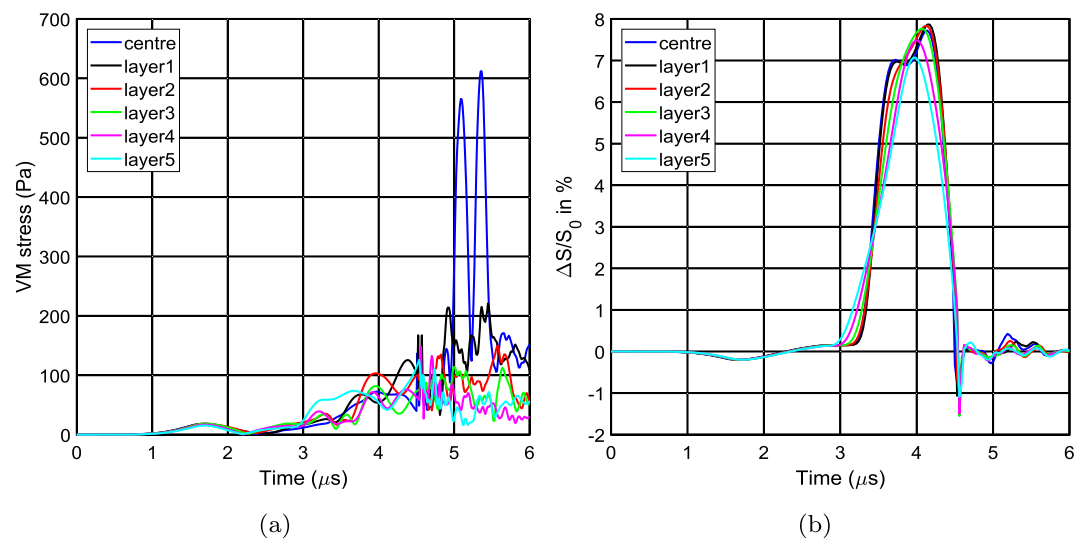

Fig. 11. Cell response simulated at the representative cell in each surrounding ring layer: (a) von Mises stress measured at the distal part of the cell; (b) membrane strain.
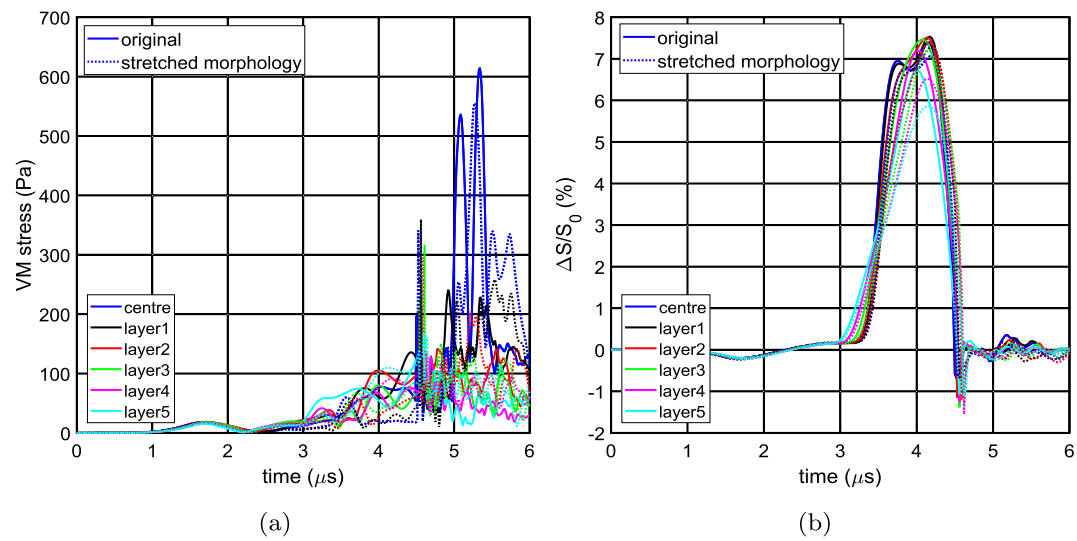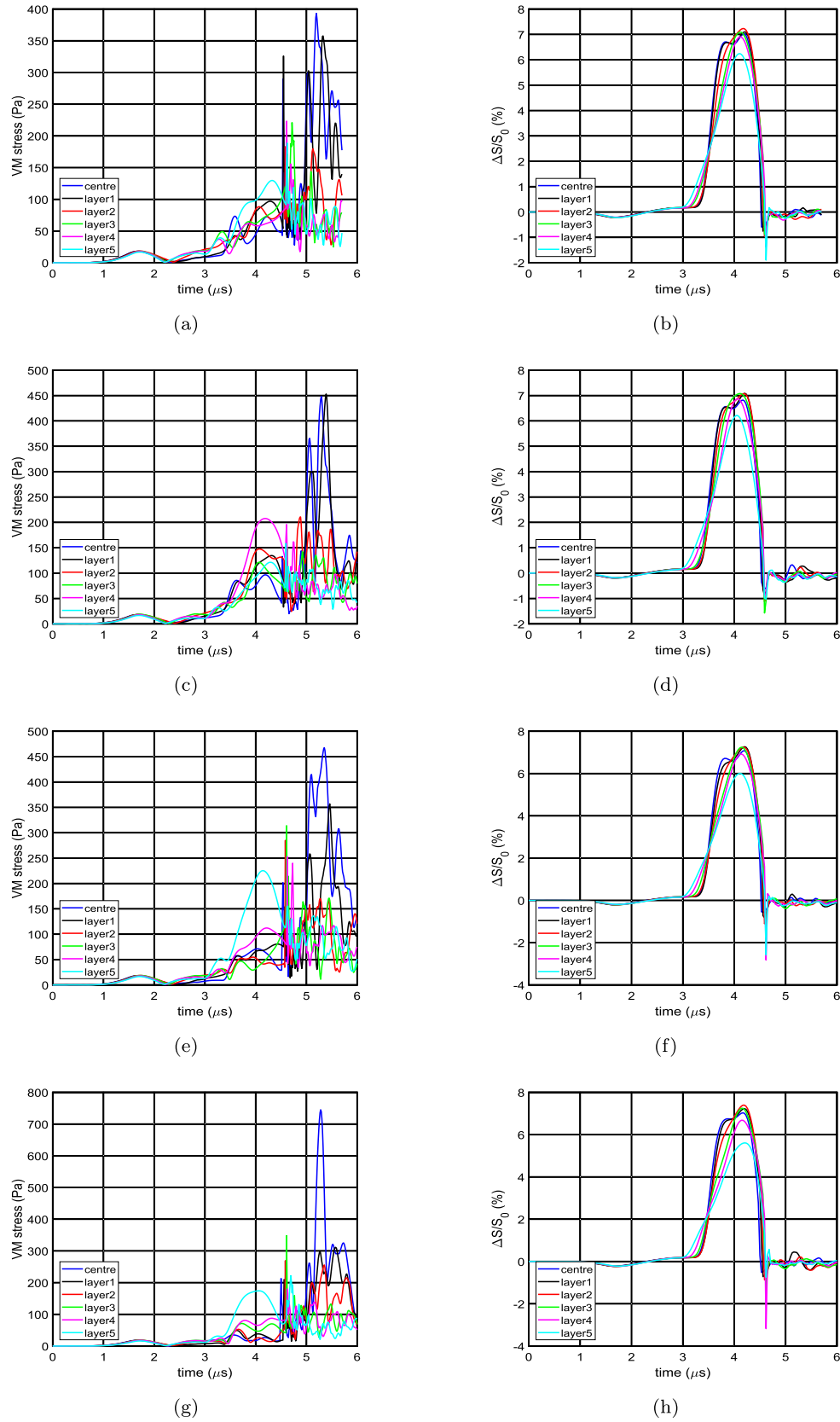

Fig. 12. Comparison of representative cell response for each ring layer between the original model and its morphologically stretched counterpart: (a) von Mises stress measured at the distal part of the cell; (b) membrane strain.

Fig. 13. Representative cell response of each ring layer for different cluster orientations: 45° (a)–(b), 90° (c)–(d), 135° (e)–(f) and 180° (g)–(h); (a), (c), (e), (g) von Mises stress measured at the distal part of the cells; (b), (d), (f), (h) membrane strain.
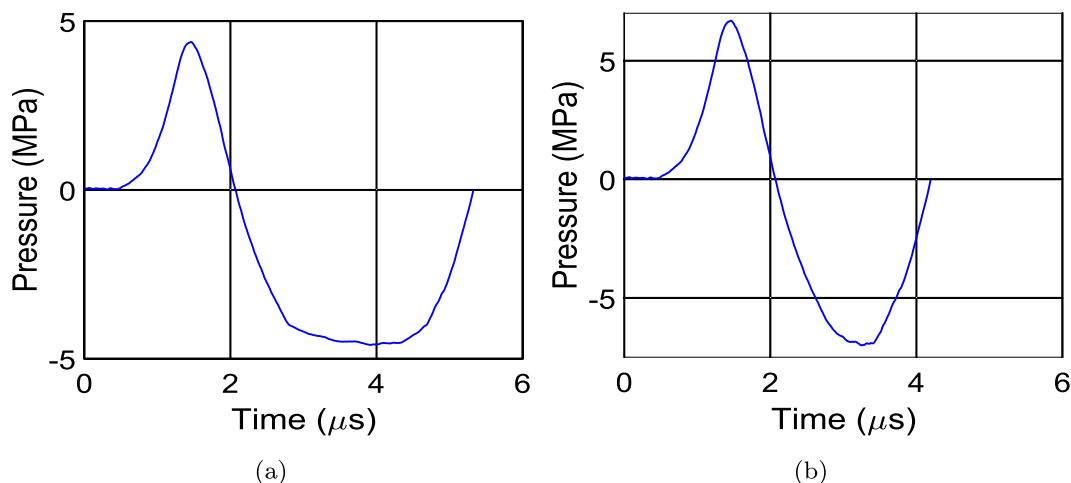
Fig. 14. Applied artificial shock wave profiles. (a) Maximum tensile pressure of 4.59 MPa; (b) maximum tensile pressure of 7 MPa.

influenced. Similar to the findings in the single cell study, the model surface curvature results in different level of von Mises stress concentration, thus the von Mises stresses are higher in the 0° and 180° cases.

4.2.4. Tumour spheroid response

Two *in silico* designed shock wave profiles were recently proposed to specifically target cancer cells while having minimal impact on normal cells at single cell level [5]. Here, the two shock wave profiles were used to study cell response in an initial tumour environment. The first shock wave profile (Fig. 14(a)) has a peak negative tensile pressure of 4.59 MPa, which exceeds the transition threshold of cancer cells but not of healthy cells, and therefore could result in specific sonoporation effect in cancer cells without damaging normal cells; the second shock wave profile with the peak negative pressure of 7 MPa (Fig. 14(b)) results in large deformation in both cancer and healthy cells, however, the rupture strain threshold for cancer cells have been reported to be around 5% [23,24] while that of healthy cells is 40% or higher [25,26]. Therefore, this shock wave profile aims to rupture cancer cells without much influence on healthy cells. See Ref. [5] for more details.

Fig. 15 shows the membrane strain of a cell at each layer of the multicellular spheroid under the two designed shock wave profiles.

Under the first shock wave (maximum tensile pressure of 4.59 MPa), compared to the response of individual cancer cells (CAKI-2) and healthy cells (HRE) in the agarose tissue phantom [5], the multicellular spheroid model results (Fig. 15 (a)) showed an increase of the membrane strain in both CAKI-2 (from 1.1% to 1.3%) and HRE cells (from <0.2% to ∼0.4%). The difference of ∼1% between the cancerous and non-cancerous cells was still preserved.

Fig. 15(b) shows the cell response using the second shock wave profile. The cell cluster showed an increased membrane strain compared to the single cell case: the measured maximum membrane area change was around 9% in the cell cluster while that in the single cell model was around 5–6%. These values still exceed the rupture strain threshold of cancer cells (3–5%) but not that of normal cells (∼40%), which may still lead to cancer cell rupture without damaging the surrounding normal cells.

5. Discussion and conclusion

This work aims to study cell interaction with shock waves in a more biophysically realistic environment. It analyses shock wave interaction with 3D cells whose geometry was obtained from microscopy of individual cells. The results showed that for a single
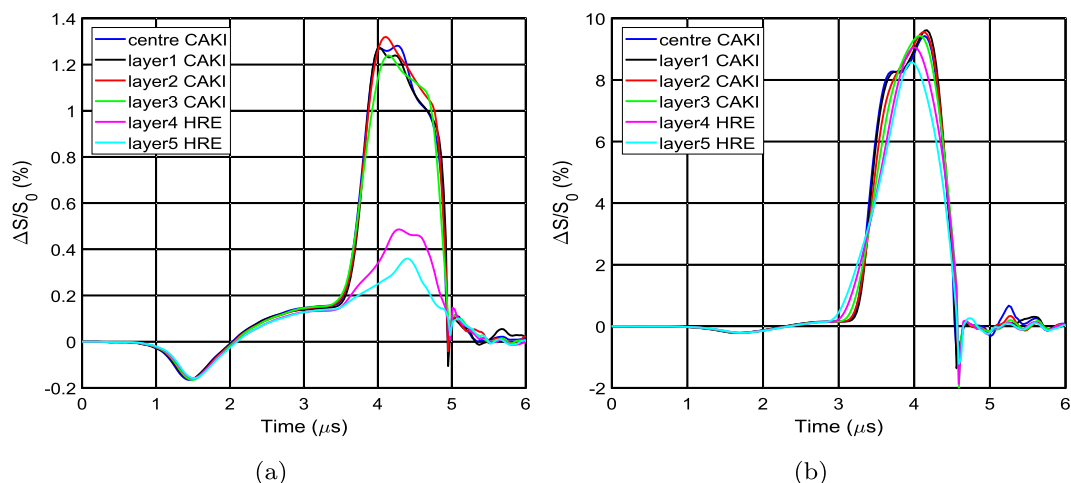

Fig. 15. Membrane strain measured at representative cells in each layer of the spheroid model under designed shock wave profile with the maximum tensile pressure of (a) 4.59 MPa; (b) 7 MPa.

cell embedded in an extracellular environment, its geometry did not strongly affect the membrane strain, but that the maximum von Mises stress could increase threefold in regions of smaller radii of curvature.

The presence of neighbouring cells was found to induce a stronger effect on the cell response to shock waves. Both the von Mises stress and membrane strain were amplified by roughly a factor of four with the presence of surrounding layers compared to a homogeneous gel. The membrane strain response of the central cell converged with more than three surrounding layers. This indicates that the cell deformation was only influenced locally by the neighbouring cells, but the von Mises stress may be more sensitive to a wider range of neighbouring cells due to the interference of stress propagation. Note that this representation is from a mechanical perspective without including the biochemical influence of the cell spheroid on cell behaviours.

The response of a multicellular spheroid model made of CAKI-2 and HRE cells was also analysed in order to study the differentiation between cancer cells and their noncancerous counterparts in a more biophysically realistic (e.g., tumour mimicking) environment. This study used two *in silico* designed shock wave profiles as in the previous single cell study [5]. Compared to the single cell study, the cell membrane strain was found to increase in both cancer and normal cells due to the effects of neighbouring cells. However, the difference in cell membrane strain increase in response to shock wave tension was still preserved between the cancer and normal cells. This phenomenon indicates that in a 3D multicellular environment, cancer cells can also be targeted with minimal interference on the surrounding healthy cells.

In conclusion, this work advances the understanding of the interaction of shock waves and cells by using more realistic environments including 3D cell morphology and the influence of neighbouring cells. The cellular morphology was found not to significantly influence the overall cell membrane strain but to influence the von Mises stress. The presence of surrounding neighbouring cells enhanced the single cell response to shock waves, which suggests that the extracellular environment is critical and that single cell experiments may not be representative of more complex biological situations. This work also showed a preliminary indication of the effects of neighbouring cells, revealing that a spheroid model with three surrounding layers should be sufficient to study the cell membrane strain embedded in tissue. However, a fully 3D model with multiple layers is called for studying the stress evaluation inside tissues. The study also confirmed that the shock wave profiles proposed in Ref. [5] also differentiated cancer cell and normal healthy cells in the multicellular spheroid environment.

Acknowledgements

Appendix A. Supplementary data

Supplementary data associated with this article can be found, in the online version, at https://doi.org/10.1016/j.actbio.2018.04.041. Finite element meshes for this article are available through the Oxford University Research Archive (ORA).

References

[1] J. A. McAteer, A. P. Evan, The acute and long-term adverse effects of shock wave lithotripsy, in: Seminars in Nephrology, 2008.
[2] C.J. Wang, An overview of shock wave therapy in musculoskeletal disorders, Chang Gung Med. J. 26 (4) (2003) 220–232.
[3] A. Maxwell, T. Wang, C. Cain, J. Fowlkes, O. Sapozhnikov, M. Bailey, Z. Xu, Cavitation clouds created by shock scattering from bubbles during histotripsy, J. Acoust. Soc. Am. 130 (4) (2011) 1888.
[4] R. Murata, K. Nakagawa, S. Ohtori, N. Ochiai, H. Moriya, The effects of radial shock waves on gene transfer in rabbit chondrocytes in vitro, Osteoarthritis Cartilage 15 (11) (2007) 1275–1282.
[5] D. Li, A. Pellegrino, A. Hallack, N. Petrinic, A. Jerusalem, R. O. Cleveland, Charaterisation of single cell response to shock waves and in silico optimisation of shock wave mediated cancer therapy, Biophys. J.
[6] M.J. Ryan, G. Johnson, J. Kirk, S.M. Fuerstenberg, R.A. Zager, B. Torok-Storb, Hk-2: an immortalized proximal tubule epithelial cell line from normal adult human kidney, Kidney Int. 45 (1) (1994) 48–57.
[7] V. Egorov, S. Tsyuryupa, S. Kanilo, M. Kogit, A. Sarvazyan, Soft tissue elastometer, Med. Eng. Phys. 30 (2) (2008) 206–212.
[8] K. Svoboda, R. Yasuda, Principles of two-photon excitation microscopy and its applications to neuroscience, Neuron 50 (6) (2006) 823–839.
[9] A. Jrusalem, M. Dao, Continuum modeling of a neuronal cell under blast loading, Acta Biomater. 8 (9) (2012) 3360–3371.
[10] M. Clausen, H. Colin-York, F. Schneider, C. Eggeling, M. Fritzsche, Dissecting the actin cortex density and membrane-cortex distance in living cells by super-resolution microscopy, J. Phys. D: Appl. Phys. 50 (6) (2017) 064002.
[11] J.E. Parsons, C.A. Cain, J.B. Fowlkes, Cost-effective assembly of a basic fiber-optic hydrophone for measurement of high-amplitude therapeutic ultrasound fields, J. Acoust. Soc. Am. 119 (3) (2006) 1432–1440.
[12] J. Simo, T. Hughes, Computational Inelasticity, Springer, 2008.
[13] L. M. Rebelo, J. S. De Sousa, J. Mendes Filho, M. Radmacher, Comparison of the viscoelastic properties of cells from different kidney cancer phenotypes measured with atomic force microscopy, Nanotechnology 24 (5) 0.
[14] A. Jérusalem, M. Dao, Continuum modeling of neuronal cell under blast loading, Acta Biomater. 8 (9) (2012) 3360–3371.
[15] M. Herant, V. Heinrich, M. Dembo, Mechanics of neutrophil phagocytosis: behavior of the cortical tension, Journal of cell science 118 (9) (2005) 1789–1797.
[16] G.E. Leclerc, L. Debernard, F. Foucart, L. Robert, K.M. Pelletier, F. Charleux, R. Ehman, M.-C. Ho Ba Tho, S.F. Bensamoun, Characterization of a hyper-viscoelastic phantom mimicking biological soft tissue using an abdominal pneumatic driver with magnetic resonance elastography (MRE), J. Biomech. 45 (6) (2012) 952–957.
[17] Amira for Life Sciences, FEI, User Manual (2014).
[18] D. Claxton, Vectorized Surface Curvature Computation, MathWorks, 2006.
[19] G. Schaller, M. Meyer-Hermann, Multicellular tumor spheroid in an off- lattice Voronoi-Delaunay cell model, Phys. Rev. E: Stat., Non-linear Soft Matter Phys. 71 (5) (2005) 1–37.
[20] M. Bock, A. K. Tyagi, J. U. Kreft, W. Alt, Generalized voronoi tessellation as a model of two-dimensional cell tissue dynamics, 72, 2010.
[21] R. Quey, P. Dawson, F. Barbe, Large-scale 3D random polycrystals for the finite element method: generation, meshing and remeshing, Comput. Methods Appl. Mech. Eng. 200 (17–20) (2011) 1729–1745.
[22] L.-B. Weiswald, G. Jean-Marc, S. Richon, D. Bellet, B. Saubama, V. Dangles-Marie, In situ protein expression in tumour spheres: Development of an immunostaining protocol for confocal microscopy 10 (2010) 106.
[23] L. Weiss, Biomechanical interactions of cancer cells with the microvasculature during hematogenous metastasis, Cancer Metastasis Rev.. 14 (2) (1992) 187–215.
[24] L. Weiss, D.S. Dimitrov, M. Angelova, The hemodynamic destruction of intravascular cancer cells in relation to myocardial metastasis, PNAS 82 (17) (1985) 5737–5741.
[25] F. Li, C.U. Chan, C.D. Ohl, Yield strength of human erythrocyte membranes to impulsive stretching, Biophys. J. 105 (4) (2013) 872–879.
[26] T. Shigematsu, K. Koshiyama, S. Wada, Effects of stretching speed on mechanical rupture of phospholipid/cholesterol bilayers: molecular dynamics simulation, Sci. Rep. 5 (2015) 15369.